



Article

Slip Models of the 2016 and 2022 Menyuan, China, Earthquakes, Illustrating Regional Tectonic Structures

Donglin Wu, Chunyan Qu ^{*}, Dezheng Zhao , Xinjian Shan and Han Chen

State Key Laboratory of Earthquake Dynamics, Institute of Geology, China Earthquake Administration, Beijing 100029, China

^{*} Correspondence: dqchy@ies.ac.cn

Abstract: As one of the large-scale block-bounding faults in the northeastern Tibetan Plateau, the Qilian-Haiyuan fault system accommodates a large portion of north-eastward motion of the Tibetan Plateau. In 2016 and 2022, two strong earthquakes of Mw6.0 and Mw6.6 occurred in the Menyuan area near the Lenglongling fault (LLLF) at the western segment of the Qilian-Haiyuan fault. These two adjoining events, only 40 km apart, exhibited notable differences in focal mechanisms and rupture kinematics, indicating complex fault geometries and tectonic structures in the region, which are still poorly known. Here, we obtained an interseismic velocity map spanning 2014–2020 in the Menyuan region using Sentinel-1 InSAR data to probe strain accumulation across the LLLF. We obtained the coseismic deformation fields of the two Menyuan earthquakes using InSAR data and inverted out their slip distributions. We calculated the Coulomb stress changes to examine the interactions and triggering relationship between two ruptures and to access regional seismic potential. We found that the 2016 earthquake was a buried thrust event that occurred on the northern LLLF, whilst the 2022 earthquake was a left-lateral strike-slip event that occurred on the western end of the LLLF. We indicated there may be no direct triggering relationship between two spatiotemporally adjacent earthquakes. However, the 2022 earthquake caused a remarkable stress perturbation to the surrounding area. Particularly, a large area with notable stress increase stands out along the Tuolaishan fault and the LLLF, likely posing a high seismic hazard in the region.

Keywords: Lenglongling fault; 2022 Menyuan earthquake; InSAR; coulomb stress change

Citation: Wu, D.; Qu, C.; Zhao, D.; Shan, X.; Chen, H. Slip Models of the 2016 and 2022 Menyuan, China, Earthquakes, Illustrating Regional Tectonic Structures. *Remote Sens.* **2022**, *14*, 6317. <https://doi.org/10.3390/rs14246317>

Academic Editors: Deliang Xiang, Ying Luo, Xueru Bai, Gangyao Kuang and Xiaolan Qiu

Received: 5 November 2022

Accepted: 9 December 2022

Published: 13 December 2022

Publisher's Note: MDPI stays neutral with regard to jurisdictional claims in published maps and institutional affiliations.



Copyright: © 2022 by the authors. Licensee MDPI, Basel, Switzerland. This article is an open access article distributed under the terms and conditions of the Creative Commons Attribution (CC BY) license (<https://creativecommons.org/licenses/by/4.0/>).

1. Introduction

The ongoing collision of the Indian and Eurasia plates has caused the expansion and uplift of the Tibetan Plateau since the early Cenozoic [1,2]. In the northeastern margin of the Tibetan Plateau, the crustal extrusion transitions from nearly northward to northeastward and eastward. The widely distributed large-scale faults host numerous major earthquakes in the region [3]. Among them, the ~900-km-long Qilian-Haiyuan fault system, with an approximate NW-SE orientation, is an active seismic zone, which is composed of the thrust-dominated northern Qilian fault (from ~98°E to ~101.3°E) and the left-lateral strike-slip Haiyuan fault (from ~101.3°E to ~106°E) (Figure 1a). The Haiyuan fault consists of the Tuolaishan (S1), Lenglongling (S2), Jinqianghe (S3), Maomaoshan (S4), and Laohushan (S5) segments, as well as the ruptured segment during the 1920 Ms8.5 Haiyuan earthquake (S6, Figure 1a) [4]. The fault slip rate of the Haiyuan fault is estimated to be 2–12 mm/yr based on geodetic and geologic studies, with a nearly linear decrease from west to east [5–13]. In the western Haiyuan fault, the Lenglongling fault is a transition zone between the northern Qilian fault and the Haiyuan fault, with several sub-parallel faults, including the Menyuan fault, the Lenglongling fault (LLLF), the Tuolaishan fault (TLSF), the northern Lenglongling fault (NLLLF), the Sunan-Qilian fault, and the Minyue-Damaying fault (MYDMYF; Figure 1b).

Two strong earthquakes (Mw6.0 and Mw6.6) occurred near the LLLF on 22 January 2016 and 8 January 2022, respectively. Their epicenters were only ~40 km apart and the

time interval between the two events was ~6 years. Nevertheless, the rupture length and focal mechanisms were notably distinct. The 2016 earthquake was dominated by thrust components with a deeper focal depth (~10 km), while the 2022 event was dominated by a left-lateral strike-slip motion with a much shallower rupture area (~5 km), which occurred to the west of the 2016 earthquake (Figure 1) [14,15]. The kinematic differences between the two spatiotemporally adjacent earthquakes may reflect the complexity of the fault system and the diversity of the deformation mode in this region. However, the regional tectonic model incorporating potential kinematic transitioning and regional fault interactions is still under debate [14,16,17].

Many studies have investigated the kinematics of the causative faults hosting the Menyuan earthquakes, relying on field investigations, geodetic observations, and relocated aftershocks [16,18–20]. The 2016 Mw6.0 Menyuan earthquake occurred to the north of the LLLF (Figure 1). Previous studies have investigated the pattern of crustal deformation and strain rate by geodetic observations before the earthquake [21,22], relocated the aftershocks [18], mapped the coseismic deformations, constrained fault geometry, and inverted coseismic slip distributions [14,23–26]. Despite the extensive studies on this event, the geometry of the source fault of the 2016 earthquake remains controversial (Table 1).

The 2022 Mw6.6 Menyuan earthquake occurred to the north of the junction of the LLLF and the TLSF. Recently, studies have reported traceable but discontinuous surface ruptures [19,27], probed the evolution of relocated aftershocks [28], documented coseismic deformation, and constrained the slip models [15,29,30]. The surface ruptures with a length of >20 km and a maximum slip of ~3.7 m have been measured based on fieldwork [19,27] and geodetic observations [29–34]. The surface ruptures have been divided into two branches. The northern branch is the main rupture and is distributed along the western LLLF, while the southern branch is distributed along the eastern TLSF.

Although many studies have been conducted, the complex fault geometry, tectonic structures, and their stress interactions in the Menyuan area are still unclear. In this work, we study the kinematic characteristics of the two events and propose a regional tectonic model. We obtain the interseismic velocity field and quantify the velocity gradient using InSAR time-series. We derive InSAR coseismic displacement fields of the two events on ascending and descending tracks, and proceed to map the surface rupture trace of the 2022 event by offset-tracking measurements. We invert the slip distribution of the two events and calculate the coseismic Coulomb stress changes due to the two events. Finally, we analyze and discuss the tectonic structures, kinematic characteristics, and stress interactions between these two earthquakes. Our results have implications for regional seismic hazard assessment.

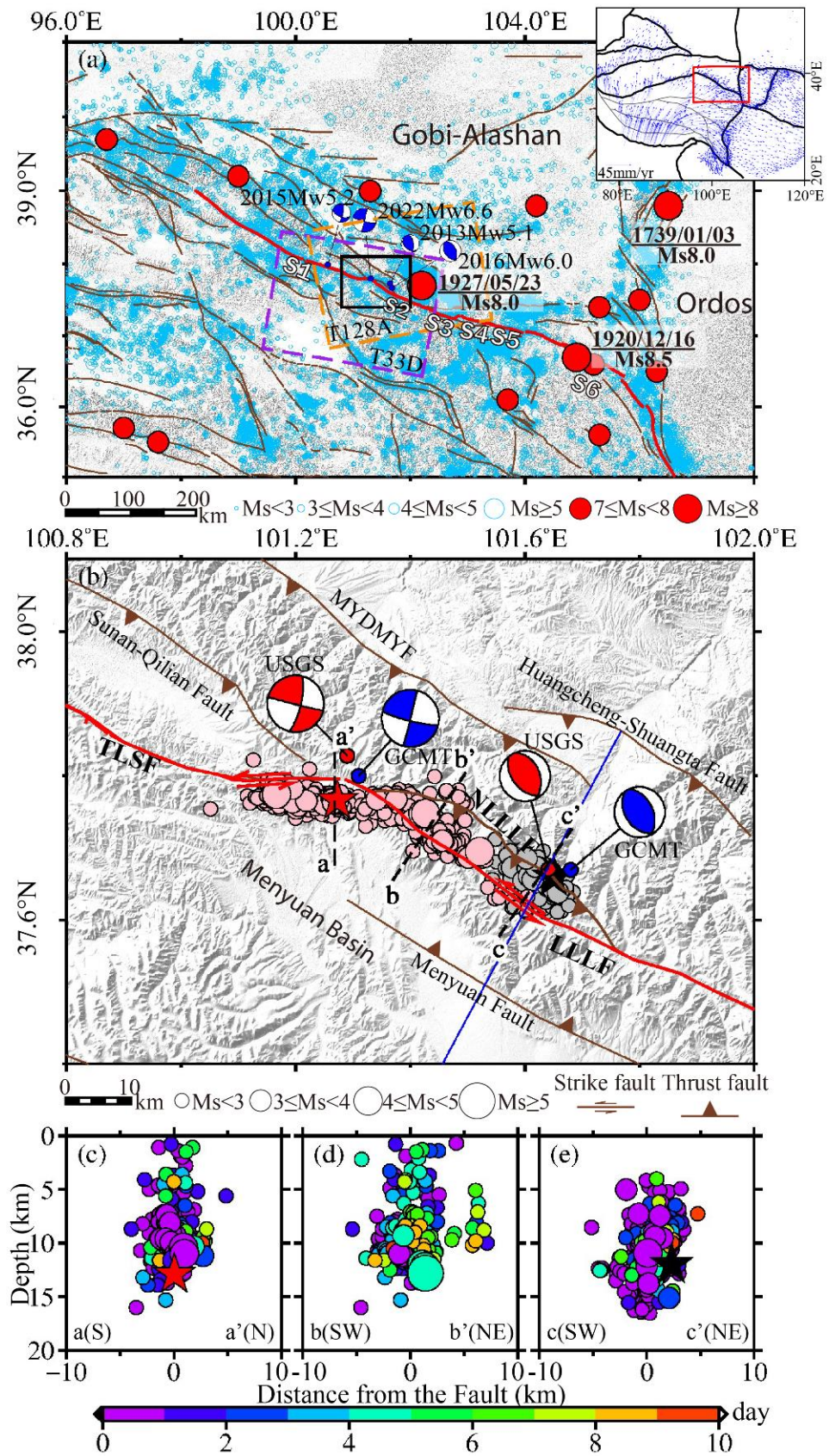


Figure 1. (a) Tectonic setting along the northeastern margin of the Tibetan Plateau. The active faults (brown lines) are from Xu et al. [35] and Guo et al. [36]. Red line marks the Qilian-Haiyuan fault system.

The blue beach balls are the GCMT focal mechanisms of earthquakes ($M_w > 5.0$) from 2012 to 2022. The light blue circles are small and moderate earthquakes ($< M_s 6.0$) between 2009 and 2020 from the China Earthquake Networks Center. Red dots show the historical earthquakes with $M_s > 7.0$. The dashed rectangles represent the footprint of the SAR data. Black rectangle outlines the extent shown in Figure 1b. The red rectangle in the inset map indicates the location of Figure 1a. The inset map shows the interseismic GNSS velocities from Wang and Shen [37]. Segments of the Qilian-Haiyuan fault system: S1: Tuolaishan, S2: Lenglongling, S3: Jinqianghe, S4: Maomaoshan, S5: Laohushan, S6: ruptured segments during the 1920 Haiyuan earthquake. (b) Faults and earthquakes in the Menyuan area. The pink and gray points represent the relocated aftershocks of the 2022 event and the 2016 event [18,28]. The red and blue beach balls are the focal mechanisms of the two Menyuan earthquakes from the USGS and the GCMT, respectively. The blue lines show the profile location of the regional tectonic model. MYDMYF: the Minyue-Damaying fault; NLLLF: the northern Lenglongling fault; TLSF: the Tuolaishan fault; LLLF: the Lenglongling fault. (c–e) Aftershock profiles along aa', bb', and cc' (width = 20km), color-coded by time after the mainshock, with profile locations shown in Figure 1b. The profile aa' and bb' are aftershocks of the 2022 event and the fault (Distance = 0) means LLLF, while the profile cc' contains aftershocks of the 2016 event and the fault (Distance = 0) means NLLLF.

Table 1. Focal mechanism parameters of the 2016 and 2022 Menyuan earthquake.

Event	Source	Longitude/°	Latitude/°	Depth/km	Mw	Strike/°	Dip/°	Rake/°
2016	USGS	101.64	37.67	9.0	5.9	141	50	79
						337	41	103
	GCMT	101.68	37.67	14.3	5.9	146	43	83
						335	47	96
	Li et al., 2016 [23]	-	-	10.5	5.9	134	43	68
	Wang et al., 2017 [17]	-	-	9	6.0	127 ± 6	45 ± 2	73 ± 6
	Liu et al., 2018 [24]	101.64	37.67	7.2	6.0	140	43	84
	Zhang et al., 2020 [14]	-	-	~13	5.9	115	50	85
	Qu et al., 2021 [26]	-	-	12	5.9	140	44	67
	This study ¹	101.60 *	37.65 *	9.25 *	6.0	127	30	70
This study ²	101.62 *	37.66 *	8.22 *	5.9	127	45	70	
2022	USGS	101.29	37.83	13.0	6.6	104	88	15
						13	75	178
	GCMT	101.31	37.80	14.8	6.6	104	82	1
						14	89	172
	Li et al., 2022 [15]	-	-	-	6.7	104	80	0
				~5		109	80	5
	Feng et al., 2022 [29]	-	-	-	6.7	88.6	70	-
				~4		127.2	88	-
	He et al., 2022 [31]	101.29	37.78	~5	6.65	108	83.6	-
	Li et al., 2022 [32]	-	-	4	6.6	106	86	-5
Luo et al., 2022 [34]	-	-	~2	6.7	106	77.6	-	
This study ³	101.28 *	37.79 *	~3.5	6.6	105	85.6	38	
This study ⁴	101.27 *	37.79 *	~3.5 *	6.6	105	85.6	38	
	101.15 *	37.79 *	~2.5 *		86			

* The parameter of the maximum slip obtained by slip inversion, ¹ the MYDMYF model, ² the NLLLF model, ³ the one-fault model, ⁴ the two-fault model.

2. Data and Methods

2.1. Interseismic Data and Processing

To characterize the strain accumulation prior to the two Menyuan earthquakes, we studied the pre-earthquake crustal deformation using InSAR and GNSS observations.

We collected the GNSS three-dimensional velocity field in the northeastern Tibetan plateau, spanning 2009–2019, in the Ordos-fixed reference frame (Figure 2a) [38].

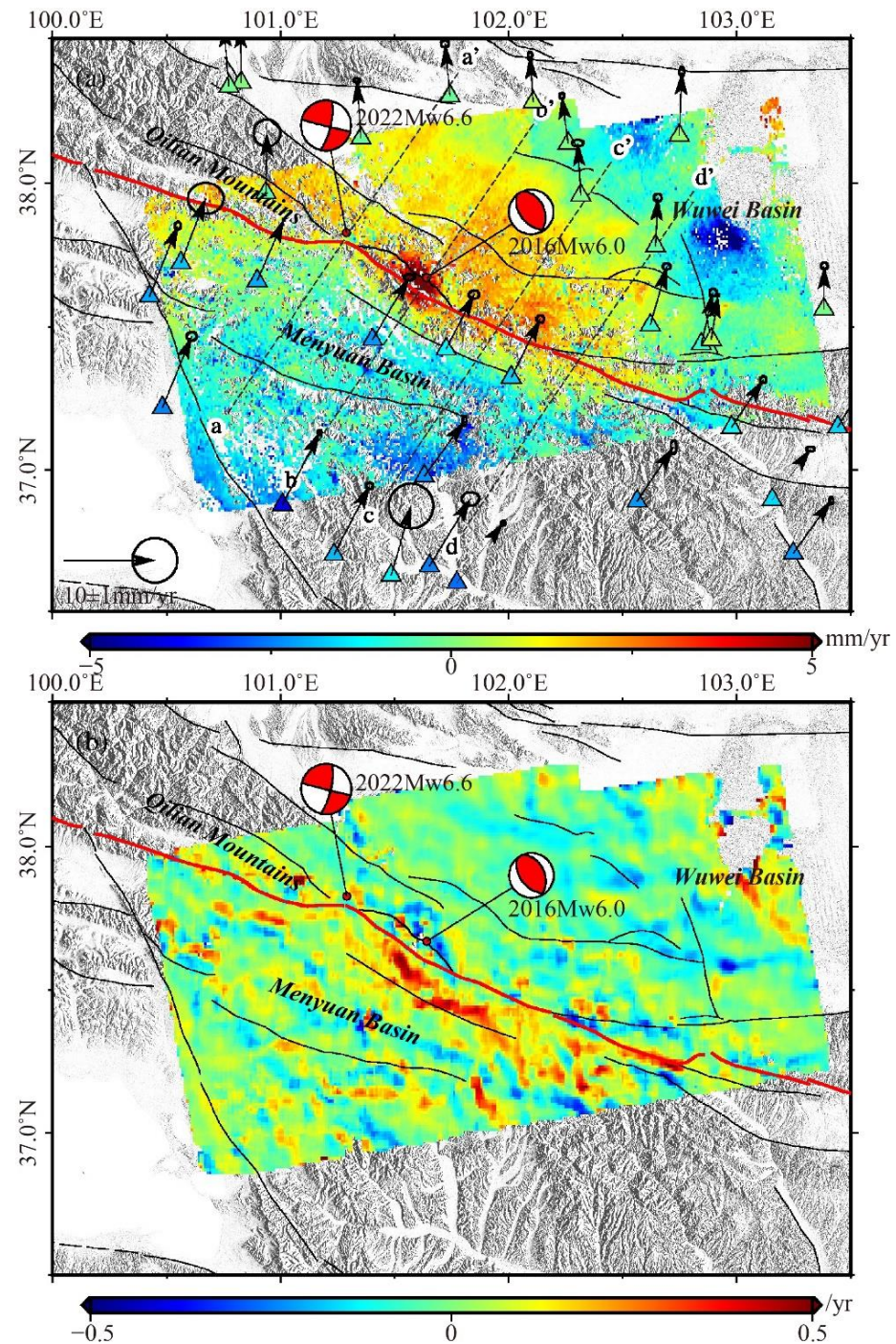


Figure 2. (a) Interseismic velocity fields of the Menyuan area from InSAR time-series in the LOS direction. (b) Velocity gradient along the N34°E direction. The red line indicates the Qilian-Haiyuan fault system. Black lines show other major faults. GNSS velocities are referenced to the stable Ordos Block [38]. The color-coded triangles represent LOS-converted horizontal velocities of GNSS data, aiding in a comparison with InSAR results.

We obtained 132 SAR images in total, spanning 2014–2020, from an ascending track (T128A) to map the interseismic velocity field over the Menyuan area. We used the ISCE software [39] to perform image registration and interferogram stack generation. The SRTM DEM with a resolution of 90 m was used to remove the topographic phase. Then, we used the StaMPS software [40] to conduct the time series inversion. Here, we focused on the mean velocity field. During the processing, we fixed the dispersion threshold amplitude at 0.4, and we used the SNAPHU to perform 3D unwrapping. Based on a multi-track orbital ramp error correction method [41,42], the residual orbit error of the InSAR LOS velocity field was mitigated by the GNSS 3D velocity field, which tied our InSAR result to the same reference frame as the GNSS data (Figure 2a). To validate our InSAR results, we compared them with the LOS-projected GNSS velocities (Figure 3).

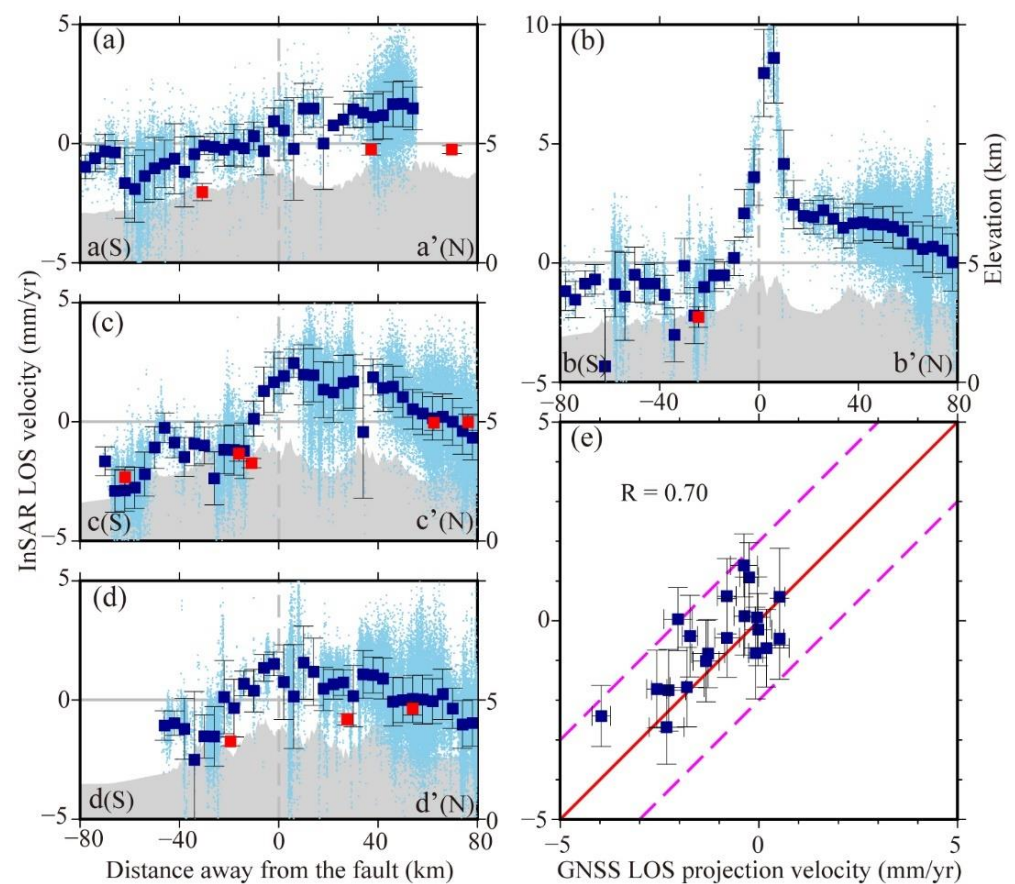


Figure 3. Comparison of InSAR and GNSS LOS-projected velocities. (a–d) The InSAR velocity profiles along aa', bb', cc', and dd' (see locations in Figure 2a). The light blue dots present the InSAR velocity (160 km long, 0.2 km wide). The dark blue squares are average values of the data within 4 km along the profiles; error bars are 1-sigma errors. The red squares present the GNSS LOS projection velocities; error bars are 1-sigma uncertainties (160 km long, 4 km wide). The light gray shadows represent the elevation along the profiles. (e) The InSAR values (y-axis) versus the GNSS values projected to LOS (x-axis). Red and cyan lines show the 1:1 relationship.

Additionally, we calculated the velocity gradient of the InSAR LOS rate map along the N34°E direction (roughly perpendicular to the strike of the LLLF). We generated a grid of $0.1^\circ \times 0.1^\circ$ and we searched the positions of points within 2.5 km along the N34°E direction for each grid point. We calculated the velocities of two points as the average velocities of 0.01o range around them, and finally, the velocity gradient of the grid point was obtained (Figure 2b).

2.2. Coseismic Data and Processing

We collected 8 Sentinel-1 SAR images from the ascending track (T128A) and the descending track (T33D), which fully covered the Menyuan seismic area, to obtain the coseismic displacement fields of the 2016 and 2022 earthquakes (Figure 1a; Table 2). We used the GAMMA software [43] to generate interferograms. We used the 1-arc-sec (30 m) SRTM DEM to remove the topographic contribution and to geocode the interferograms. We multilooked and filtered the interferograms to improve the coherence and reduce phase noise. We unwrapped the interferograms using the Minimum Cost Flow (MCF) algorithm.

In addition, we derived the range offsets using offset tracking technology [44,45] to measure the displacement in the near-field of the surface rupture of the 2022 earthquake, which has been reported to have clear surface ruptures [19,27]. We drew on spatially dense observations from range offset maps to identify the trace of surface ruptures and to construct the fault model. Since the range offset measurements have larger uncertainties than the InSAR results [20], we did not consider the offset measurements as model constraints in our following inversion for the distributed fault slip.

Table 2. Parameters of the SAR images for the 2016 and 2022 earthquakes.

Events	Orbit	SAR Image Acquisition		Perpendicular Baseline (m)	Incidence (°)	Heading (°)
		Reference	Secondary			
2016	S1 T128A	13 January 2016	6 February 2016	13	33.677	−13.238
	S1 T33D	18 January 2016	11 February 2016	5	33.729	−166.776
2022	S1 T128A	5 January 2022	17 January 2022	54	33.678	−13.237
	S1 T33D	29 December 2021	10 January 2022	39	33.706	−166.777

S1: Sentinel-1. A: ascending track. D: descending track.

2.3. Fault Model

Before kinematic inversion, we first determined the geometry of the causative fault of the two earthquakes informed by the InSAR deformation field, relocated aftershocks, field investigation, and focal mechanisms. For the 2022 Menyuan earthquake, a clear surface rupture zone has been reported [19,30]. Therefore, we remotely mapped the rupture trace from the offset-tracking results (Figures 4e and 5). We found that the eastern surface rupture was spatially consistent with the well-known LLLF in the Menyuan area. We concluded that the 2022 earthquake ruptured the LLLF. Our first model for the 2022 Menyuan earthquake included only the LLLF.

The cluster and distribution of relocated aftershocks further showed that two fault segments with varied geometries may have been involved in the rupture (Figure 1b). Inspired by this observation, we further established a two-fault model for the 2022 Menyuan earthquake. The primary strand of the fault had a curved fault geometry based on the identified rupture trace and the secondary fault strand was the southern branch in the west end of the main rupture, clearly revealed by the aftershocks and field investigation (Figures 4e and 5) [19,28].

The 2016 earthquake did not rupture to the surface, and it is challenging to robustly constrain the fault geometry of this earthquake relying on the geodetic data alone [14,16,17]. From the existing active tectonic map, the epicenter of the 2016 earthquake was located between the LLLF and the MYDMYF, but closer to the LLLF (Figure 1b). The aftershocks profile shows that the fault plane is relatively steep (Figure 1e). Constrained by geodetic observations, aftershocks, or other observations, some studies have argued that the seismogenic fault of the 2016 earthquake is the SW-dipping MYDMYF [14,25], some studies have favored the NE-dipping LLLF as the seismogenic fault [46], and other studies propose that the causative fault is more likely a secondary SW-dipping thrusting fault on the northern side of the LLLF, also called the northern Lenglongling fault (NLLLF) [16,18,24,36]. In this study, we simplified the MYDMYF and the NLLLF as two candidate faults. We constructed two single-fault models and each model incorporated one fault only. We compared the data fitting to discriminate the possible seismogenic fault of this earthquake.

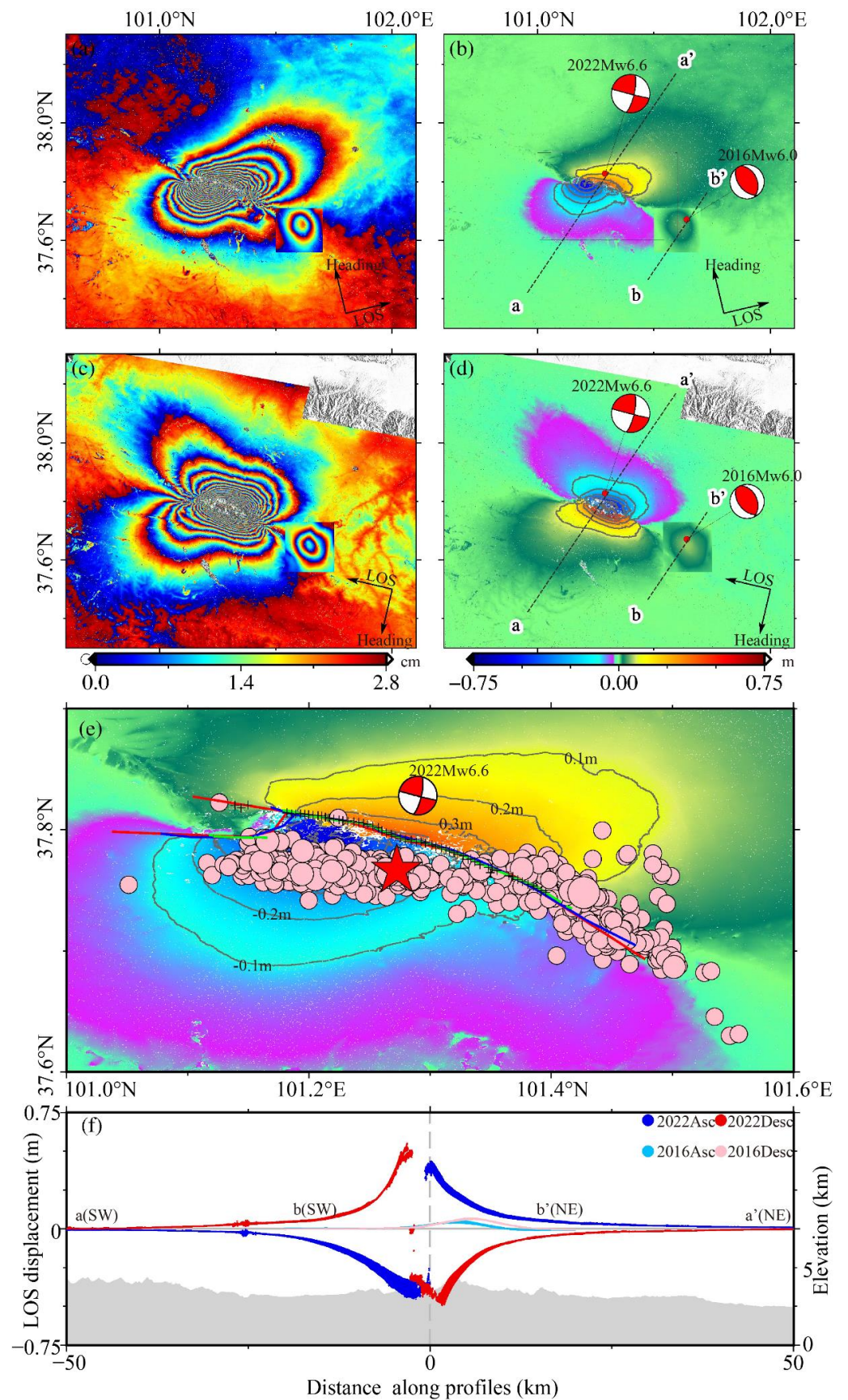


Figure 4. The collage of InSAR coseismic displacement field of the 2016 and 2022 Menyuan earthquakes. (a,c) the wrapped interferograms on ascending and descending tracks. (b,d) the corresponding

unwrapped displacement fields. The dashed black lines represent the profile locations. The black solid rectangle in (a) outlines the extent shown in Figure 4e. (e) the close-view of displacement field of the 2022 event. The pink dots are the relocated aftershocks triggered by the 2022 event [28]. The green lines present the surface rupture trace from the field investigation [19]. The blue lines represent the InSAR-derived fault trace [20]. The black cross is the surface rupture interpreted by Gaofen-7 images [33]. The red lines present the surface trace of the two-fault model for the 2022 event in this study. (f) the coseismic displacement profiles along aa' and bb' with locations shown in Figure 4b,d. The blue and red dots represent the coseismic displacement data of the ascending and descending tracks, respectively.

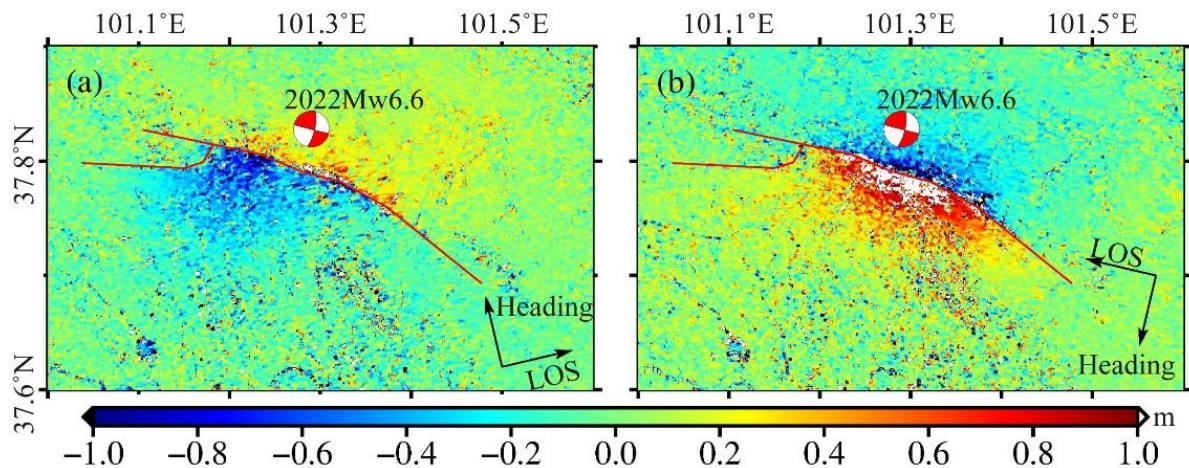


Figure 5. Surface rupture trace of the 2022 earthquake mapped based on the range offset measurements. (a,b) are the range offset results on the ascending and descending tracks, respectively. The red lines are the two-fault model of the 2022 earthquake.

2.4. Fault Slip Distribution Inversion

We used the Steepest Descent Method (SDM) [47] to invert the coseismic slip of the 2016 and 2022 Menyuan earthquakes under geodetic constraints from the LOS coseismic deformation data on both ascending and descending tracks (Figures 6 and 7). We calculated Green's function in the homogeneous elastic half-space with a Poisson's ratio of 0.25. To suppress ambient noises and to improve efficiency, we masked unreliable observations in the near-field of the fault possibly caused by phase decorrelation and unwrapping errors. We then downsampled the InSAR LOS deformation field following the DistMesh algorithm (Figure 8a–d) [48].

The fault plane was discretized into a series of sub-fault patches with a dimension of $1 \text{ km} \times 1 \text{ km}$. We allowed the rake angle of slip vectors to vary in the range of 70° to 120° for the 2016 event, and in the range of -45° to 45° for the 2022 event, respectively. We used the grid search method to find the best-fitting dip angle, allowing the dip angle to vary in a range of $20\text{--}60^\circ$ and $60\text{--}90^\circ$ for the Menyuan earthquake in 2016 and 2022, respectively. We selected the optimal smoothing factor by the L-curve between the roughness and misfit of the inversion results. The Root Mean Square is defined as:

$$RMS = \sqrt{\frac{\sum_{i=1}^m (d_{obs}^i - d_{pre}^i)^2}{m}}$$

where d_{obs}^i and d_{pre}^i are the observed and predicted surface displacements, respectively.

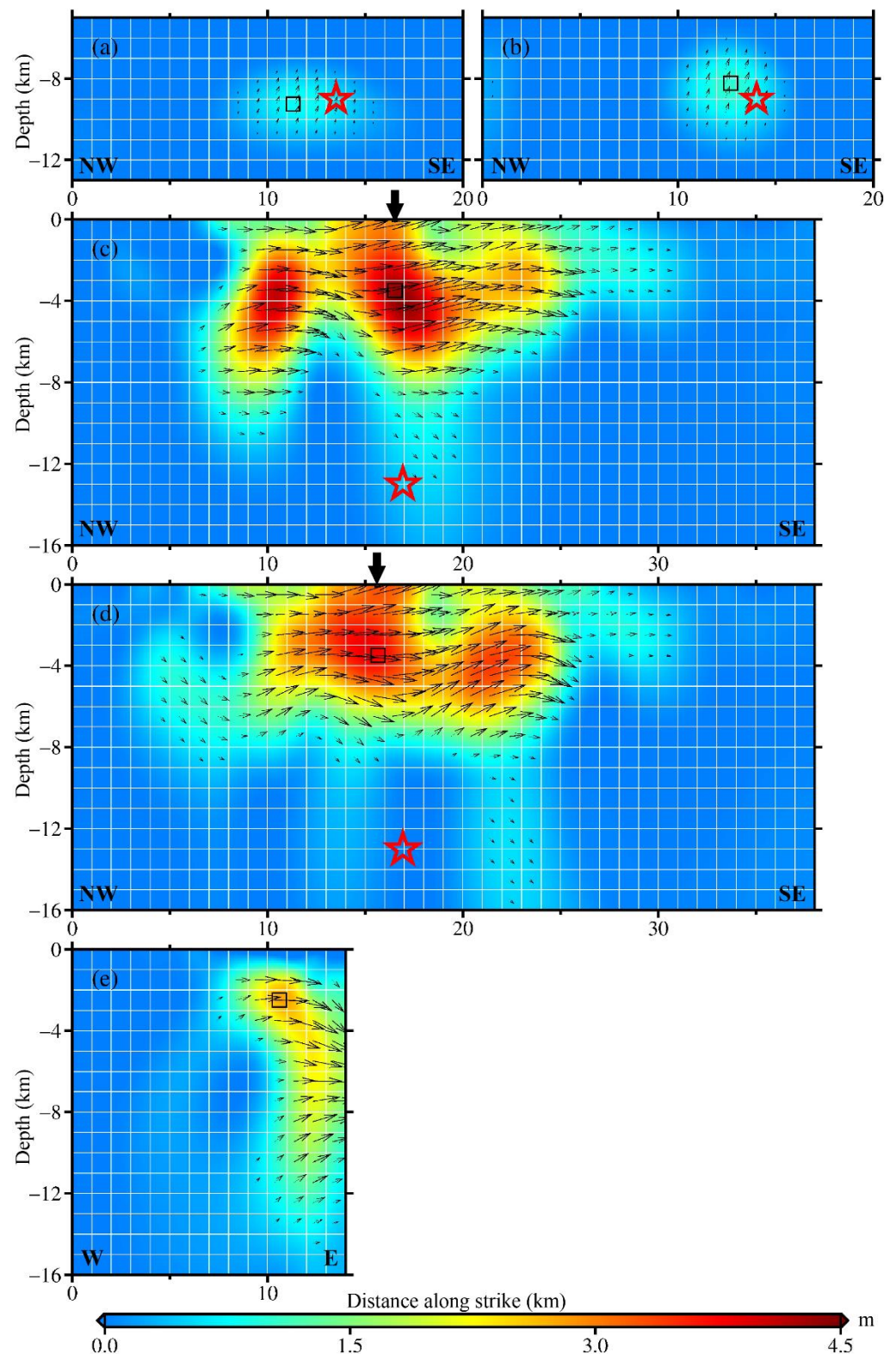


Figure 6. Slip distribution of the 2016 and 2022 Menyuan earthquakes. (a,b) the resultant slip distribution of the 2016 earthquake using MYDMYF and NLLLF as the candidate causative fault, respectively. (c) the inverted slip distribution of the 2022 earthquake for the one-fault model. (d,e) the resolved slip distribution of the 2022 earthquake for the two-fault model. Red star denotes the epicenter from the USGS. Black squares mark the location with the maximum slip. The black arrow shows the location with maximum near-surface slip.

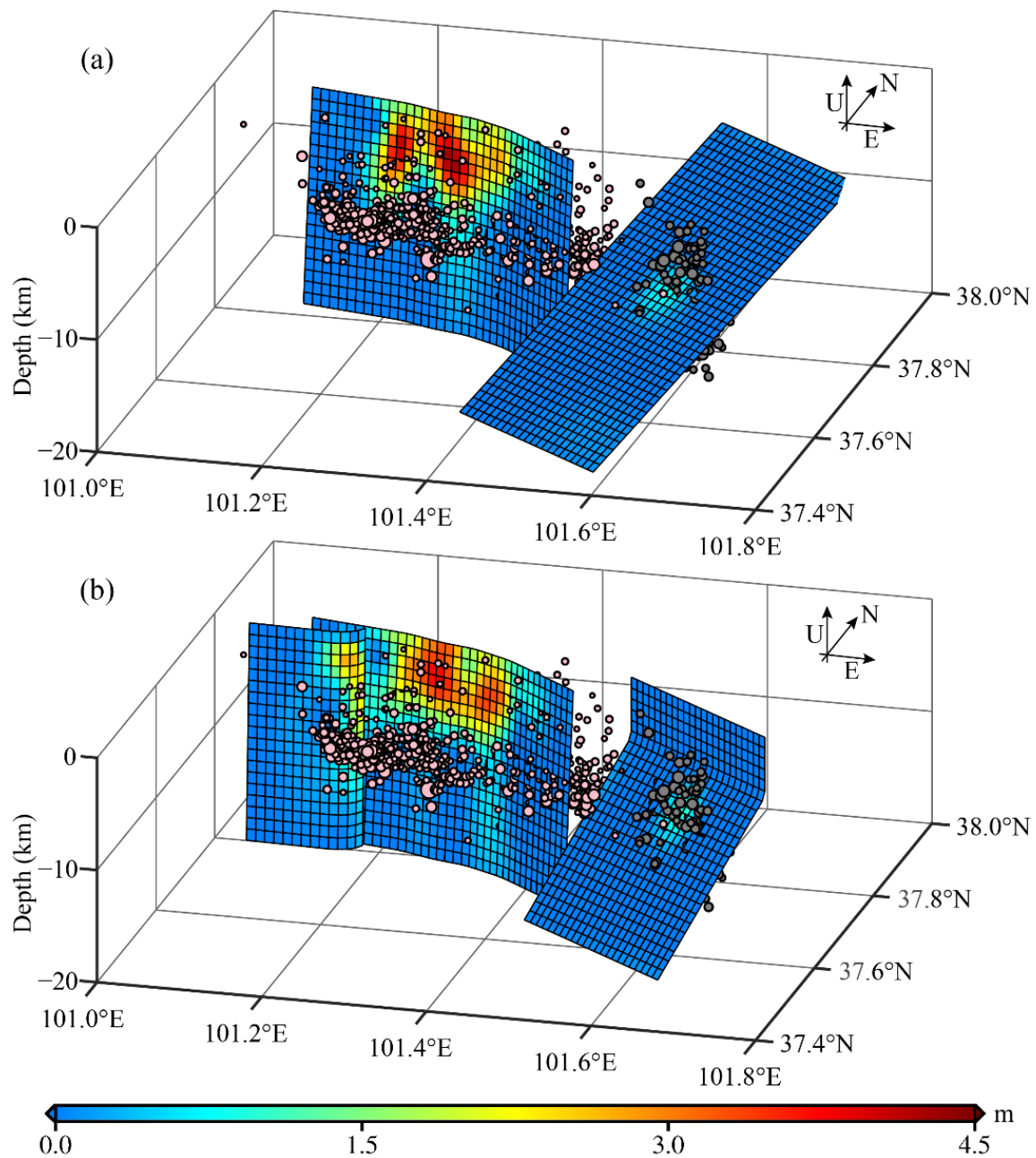


Figure 7. Three-dimensional view of the slip distribution collage obtained from different fault models of the 2016 and 2022 Menyuan earthquakes. (a) The MYDMYF model for the 2016 earthquake and the single main fault model for the 2022 event. (b) The NLLLF model for the 2016 event and the two-fault model for the 2022 earthquake. The pink and gray circles are the relocated aftershocks of the 2022 and 2016 earthquakes [18,28].

2.5. Coulomb Stress Changes Calculations

The coseismic rupture of an earthquake could modify the stress state in the adjacent lithosphere, which may affect the evolution of regional seismicity [49]. The Coulomb failure stress has been widely used in earthquake triggering analysis and long-term earthquake potential assessment [50–53]. The Coulomb failure stress change (ΔCFS) can be defined as:

$$\Delta\text{CFS} = \Delta\tau_s + \mu\Delta\sigma_n$$

where $\Delta\tau_s$ is shear stress change on the receive fault caused by an earthquake, $\Delta\sigma_n$ is the normal stress change and the tension is positive, and μ is the coefficient of friction, which is typically between 0.2 and 0.8 [54,55].

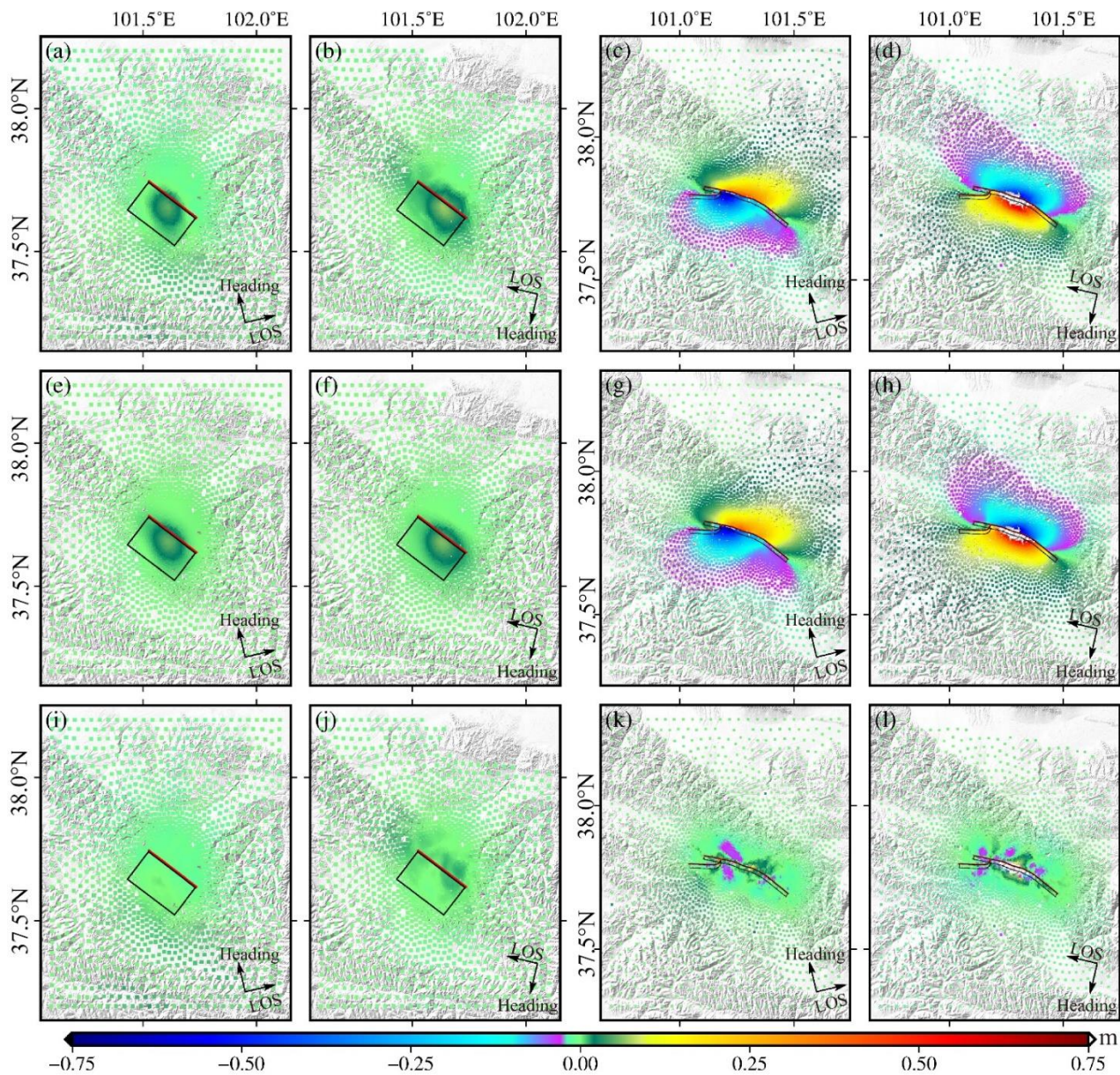


Figure 8. (a,b) Observations, (e,f) predictions, (i,j) residuals from the NLLLF model of the 2016 event on the ascending and descending tracks, respectively. (c,d) Observations, (g,h) predictions, (k,l) residuals from the two-fault model of the 2022 event. The solid red line marks the surface projections of the up-dip edge of the fault model. The black rectangle indicates the surface projection of the upper wall of the fault model.

To explore whether the 2016 event promoted or triggered the 2022 earthquake and how the seismic risk may change after these two events, we calculated the ΔCFS caused by the two earthquakes using the PSGRN/PSCMP software [56]. We take the fault slip distribution of the two earthquakes as the source fault, and the fault geometry of the 2022 Menyuan earthquake obtained by our inversion as the receiving fault. Considering that aftershocks are mainly distributed at a depth of 5–15 km, we computed the stress variation at 5 km and 10 km depths. During processing, the friction coefficient was set as 0.4, and the shear modulus was set as 30 GPa [57,58].

3. Results

3.1. Interseismic Velocity Field from InSAR over Menyuan Area

Figure 2 shows the InSAR velocity field and the gradient along the N34°E direction (roughly perpendicular to the strike of the LLLF). The notable LOS subsidence areas are mainly distributed to the SW and NE of the LLLF, associated with the basin region (Figure 2a), while LOS uplift appears in the middle of the velocity field (Figure 2a). The transition between the uplift and subsidence in LOS is smooth overall, and no velocity steps are identified (Figure 3a–d). The subsidence–uplift–subsidence pattern coincides with the expected deformation due to the subsidence of the basin (the Menyuan basin to the north and the Wuwei basin to the south) and the uplift of the Qilian Mountains under a NE compression (Figures 2a and 3c,d). The remarkable localized uplift deformation in Figures 2a and 3b is ascribed to the coseismic deformation of the 2016 Menyuan earthquake. The significant velocity gradient with a linear pattern presents a strong correlation with the LLLF, where the two Menyuan earthquakes occurred (Figure 2b).

To verify the InSAR interseismic observations, we projected the GNSS three-dimensional velocity field to the LOS direction (Figures 2a and 3). We calculated the mean velocity of InSAR points with a radius of 5 km around each GNSS site and compared them with the GNSS LOS-converted measurements. The difference between InSAR and GNSS observations was within ± 2.8 mm/yr, and the two types of observations were significantly correlated, with a correlation coefficient of 0.70 (Figure 3e).

3.2. Coseismic Displacement Field

Figure 4a–d shows the wrapped and unwrapped coseismic interferograms of the 2016 and 2022 Menyuan earthquakes on ascending and descending tracks. The deformation maps of the 2016 event display similar patterns to previous studies, showing uplifts of ~ 0.05 m in LOS on the ascending track and ~ 0.07 m in LOS on the descending track, which implies a dominant vertical displacement, produced by the thrust motion (Figure 4b,d) [14,23,24].

The coseismic deformations of the 2022 earthquake on both ascending and descending tracks are roughly symmetric with a butterfly-shaped pattern, indicating that the seismic fault may be nearly vertical. The maximum LOS displacement is ~ 0.7 m, and the maximum peak-to-trough displacement is ~ 1.2 m (Figure 4b,d,f). The flip of the sign in LOS between ascending and descending displacement fields implies a dominant horizontal displacement produced by a left-lateral strike-slip fault. The pattern of the ascending and descending fringes is similar on the southern side of the fault, but greatly differs on the northern side (Figure 4a,c).

Figure 5 shows the range offset measurements resolved by the offset-tracking method. The maximum relative displacements between two sides of the fault on the ascending and descending tracks are ~ 1.5 m and 1.2 m, respectively. All the observations reveal a generally consistent and rather clear surface rupture trace with a SEE orientation and a length of >30 km.

3.3. Coseismic Slip Distribution

To investigate the seismogenic fault of the 2016 Mw6.0 Menyuan earthquake, we take the Minyue–Damaying fault (MYDMYF) and the northern Lenglongling fault (NLLLF) as two candidate seismogenic faults for slip inversion. Our first slip model includes the MYDMYF, a south-dipping fault with a dip angle of 30°. The preferred slip model was resolved using the optimal smoothing factor of 0.01. The coseismic slip was dominated by thrust component and was confined at 6–12 km depth with a maximum value of ~ 0.8 m at a depth of 9 km (Figure 6a). The data-model correlation (DMC) for our first slip model is 0.93, and the RMS is 0.005.

Our second slip model includes the NLLLF, a south-dipping fault with a varied dip angle from 90° at shallow to 45° at depth. The optimal smoothing factor, corresponding to our preferred slip model, is 0.005. The slip distribution and the pattern were roughly akin to the first model using MYDMYF, but the amplitude of coseismic slip varies. For

instance, the maximum fault slip was ~1 m at a depth of ~8 km (Figure 6b), larger than that in the first model. Although the DMC and RMS of the two models are comparable (Figures 8i,j and S1i,j), the dip of NLLLF matches the fault geometry from relocated aftershocks (Figures 1e and 7). Therefore, we favor that the NLLLF hosted the 2016 earthquake.

For the 2022 Menyuan earthquake, we inverted the slip distribution based on the one-fault and two-fault models (Figure 6c–e). Figure 6c shows the coseismic slip distribution of the 2022 Menyuan earthquake using a one-fault model with a dip angle of 85.6° and a smoothing factor of 0.025. The coseismic slips on the fault plane are multi-peaked, mostly confined at a depth of >12 km, and dominated by the left-lateral strike-slip component. The maximum slip of ~4.5 m is located at 3.5 km depth. The maximum near-surface slip is ~3.0 m (Figure 6c). The resolved moment magnitude is Mw6.6. Residuals of InSAR data for the one-fault model are subtle and the RMS is 0.027, but significant residuals with interesting patterns on the west end of the fault (Figure S1k,l) indicate coseismic slip on a branch fault there, justifying the two-fault model.

The inversion results of the two-fault model are shown in Figure 6d,e. We resolve two main slip areas (Figure 6d), mainly the left-lateral strike-slip component with a minor dip slip. We find one concentrated slip area dominated by the left-lateral strike-slip component on the western branch fault (Figure 6e). The peak slip on the main fault is 3.8 m at a depth of 3.5 km. The maximum near-surface slip of 3.2 m appears at (101.27°E, 37.79°N) (Figure 6d). The corresponding moment is 8.89×10^{18} Nm, equivalent to a moment magnitude of Mw6.6. The RMS is 0.015. The data-fitting was slightly improved by the two-fault model (Figure 8k,l).

3.4. Coulomb Failure Stress Change

Based on the preferred coseismic slip models of two earthquakes, we calculated the Δ CFS caused by the 2016 Menyuan earthquakes on the causative fault hosting the 2022 earthquake and the Δ CFS imposed by the 2022 earthquake in the whole Menyuan area. The results are shown in Figure 9. The stress-loading areas (positive Δ CFS) caused by the 2016 earthquake are roughly located along the NLLLF with a trending of NW-SE (Figure 9a,b). The 2022 earthquake was located at the stress loading areas, but the amplitude of the Δ CFS was smaller than 0.002 MPa, which is below the widely accepted triggering threshold (0.01 MPa) [51]. We admit that increasing the coefficient of friction in the calculation will lead to a larger Δ CFS, but still below the triggering threshold. The result implies that the 2016 thrust earthquake may not have triggered the 2022 strike-slip earthquake. Figure S2a,b shows that most aftershocks of the 2016 event occurred around 10 km depth, and >60% of aftershocks occurred in the stress shadows of the mainshock, indicating that most aftershocks are not triggered by the 2016 earthquake. The cluster of aftershocks may arise from the post-earthquake processes (i.e., afterslip) or a high level of interseismic stress accumulation in this region [21,59].

Four significant stress-loading areas imposed by the 2022 earthquake are identified. Two of them are distributed near the northern and southern sides of the epicenter, and the others are located along the TLSF and the LLLF (Figure 9c,d). The coseismic Δ CFS on the TLSF, the LLLF, and the NLLLF are stress-loading, and their interseismic slip rates are estimated to be ~3 mm/yr with a low level of seismicity [4], indicating a seismic hazard on these seismic gaps (Figure 9c,d). We also find that >50% of the aftershocks of the 2022 earthquake occurred around 10 km and mostly were in the stress-increasing zone, suggesting a significant triggering effect of the mainshock on the aftershocks (Figure S2c,d).

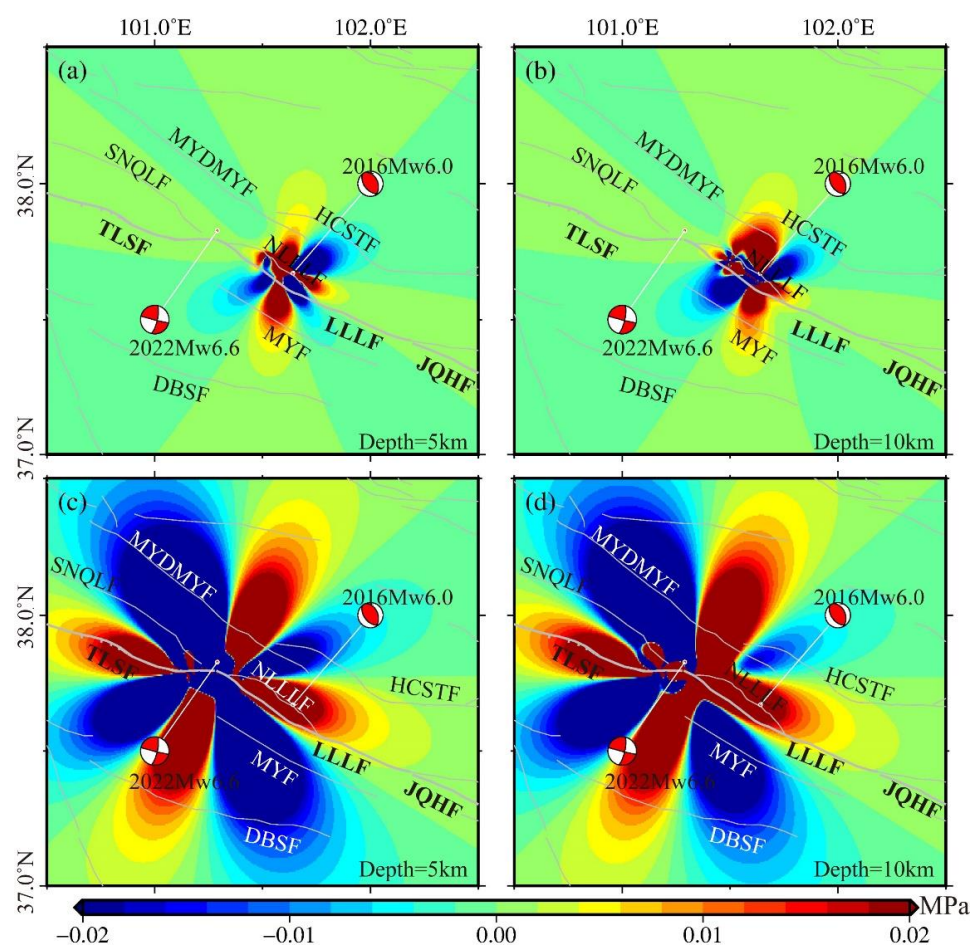


Figure 9. Distribution of Δ CFS caused by the 2016 and 2022 Menyuan earthquakes at depths of 5 km and 10 km. (a,b) Δ CFS caused by the 2016 earthquake, (c,d) Δ CFS caused by the 2022 earthquake. HCSTF: the Huangcheng-Shuangta fault; MYDMYF: the Minyue-Damaying fault; SNQLF: the Sunan-Qilian fault; NLLLF: the northern Lenglongling fault; TLSF: the Tuolaishan fault; LLLF: the Lenglongling fault; JQHF: the Jinqianghe fault; MYF: the Menyuan fault; DBSF: the Dabanshan fault.

4. Discussion

4.1. Seismogenic Faults of the Two Menyuan Earthquakes Linked to the Regional Tectonic Structures

The LLLF is situated in the complex transition zone between the strike-slip Haiyuan fault and the thrust northern Qilian fault. There are several NW-striking faults with different kinematic characteristics, varied fault geometry, and tectonic partitioning between strike-slip and dip slip. For instance, the LLLF dips nearly upright but slightly SW; the MYDMYF has a relatively small dip angle and dips SW. We studied the fault geometry and kinematics of the NLLLF and the Menyuan fault (Figure 10) in the region. The seismogenic structure of the two Menyuan earthquakes can be linked to the structural morphology and kinematic characteristics in this region.

Our slip models of the 2022 Menyuan earthquake are consistent with previous studies [15,29], and they determine the near vertical LLLF as the main seismogenic fault. Our study further inspected the rupture kinematics on the southwestern branch fault. The dip angle of the branch fault is $\sim 85^\circ$, which corresponds to its steepness in the shallow crustal revealed by high-resolution seismic-reflection and magnetotelluric profiles (Figure S3) [60–63]. The addition of the southwestern branch fault did not influence the slip pattern on the main fault, but it can improve the data-fitting (Figures 6c–e, 8k,l, and S1k,l).

We note some differences in the slip models of the 2016 Menyuan earthquake between our studies and previous studies (Table 1) [17,23,24]. Since this earthquake did not rupture

the surface, limited InSAR observations are not capable of robustly constraining fault geometries. It is helpful to analyze the geological data and aftershocks to better constrain the fault geometry. Geological studies imply that the LLLF is a left-lateral strike-slip fault, which excludes the possibility of the seismogenic fault hosting the 2016 earthquake. Most studies have proposed that the seismogenic fault hosting the 2016 event was the NLLLF, to the north side of the epicenter [16,23,24], while other studies have argued that the MYDMYF produced this event [14,25]. Our best-fitting results show that the MYDMYF has a dip angle of $\sim 30^\circ$, which is much smaller than that given by the geological inference of a dip of $\sim 60\text{--}70^\circ$ (Figure 10).

The NLLLF is an active fault, determined by remote sensing images and field studies, which is undergoing the left-lateral shear and convergence at the western end of the LLLF (Figure S4) [36]. Our preferred fault dip angle (45°) is well consistent with the aftershock distributions (Figures 1e and 10). Consequently, we favor the slip model that the NLLLF is the seismogenic fault of the 2016 Menyuan earthquake (Figure 10).

Based on the resolved fault geometry, combined with the relocated aftershocks and geological studies, we propose the regional structural schematic maps associated with the two Menyuan earthquakes, shown in Figure 10. We envision that the NLLLF soles into the LLLF in the deep crust, and the two faults with the orientation of SW may constitute a positive flower structure and be connected to a deeper large-scale detachment fault (Figure S5) [64,65].

At the northern Qaidam Basin, which has a similar tectonic setting to the Menyuan region, two moderate earthquakes of similar magnitude ($\sim \text{Mw}6.4$) have occurred at a short time interval [66,67]. The earthquake that occurred in November 2008 ruptured the lower part (10–23 km) of the seismogenic fault, while the earthquake in August 2009 ruptured the upper part (<10 km) [67]. These two earthquakes have good spatial complementarity, and the first event triggered the latter one from the Coulomb stress changes [66]. The flower structure at depth may prevent the rupture of the deep earthquake from propagating upwards to form shallow slip deficits, and the accumulation of Coulomb stress caused by the deep event may greatly increase the possibility of destructive earthquakes in the shallower fault in a short time [66,67]. This may also have been one of the mechanisms of the 2022 Menyuan earthquake.

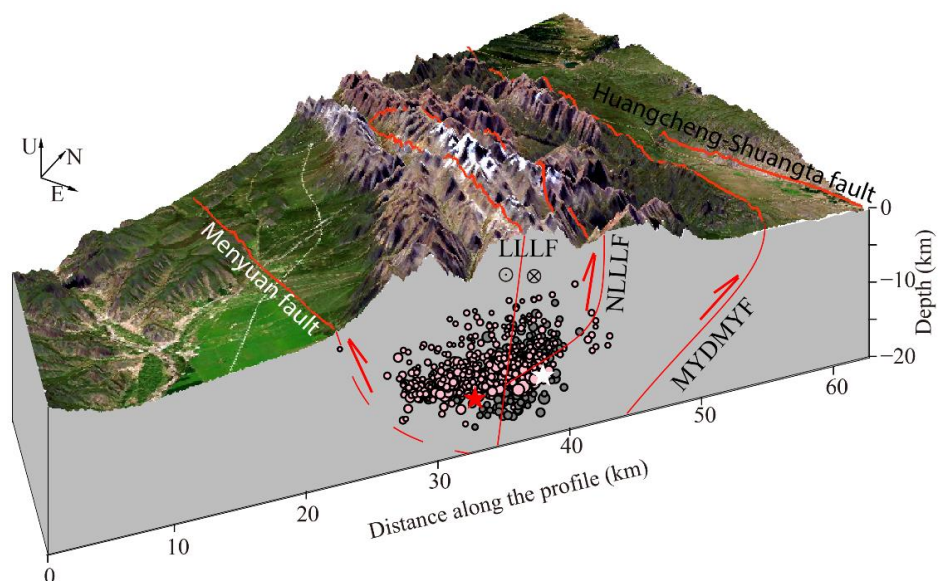


Figure 10. The regional tectonic model illuminated by the two Menyuan earthquakes. The profile location is shown in Figure 1b with a blue line. Gray and pink dots represent the aftershock relocations of the 2016 and 2022 Menyuan earthquakes. Red lines show the active faults, and red dashed lines show the inferred fault location.

4.2. Relationships between Two Menyuan Earthquakes and Regional Seismic Hazard

Large earthquakes often alter the stress state in the surrounding lithosphere, either loading nearby faults to promote the occurrence of future earthquakes or unloading these faults to inhibit or delay future earthquakes [55]. The 2016 and 2022 Menyuan earthquakes were ~40 km apart, however, their focal depth, fault geometry, and kinematic properties were significantly diverse. As suggested by the Coulomb stress calculations (Figure 8a,b), the spatial extent of stress variation caused by the 2016 earthquake is very limited. The area with increased stress of >0.01 MPa is mainly distributed at the NLLLF and the west end of LLLF, while it has little impact on other surrounding faults. Although the coseismic deformation of the 2016 event produces positive Δ CFS on the epicenter of the 2022 event at both depths of 5 km and 10 km, the amplitude is smaller than 0.01MPa (Figure 8a,b), which may not be sufficient to promote the occurrence of the 2022 event. We conclude that the 2022 Menyuan event resulted from other or multi mechanisms, such as long-term interseismic stress accumulation, rather than only being triggered by the 2016 earthquake.

The Δ CFS caused by the 2022 event is widely distributed in the adjacent area. The stress perturbation to the regional stress field is much larger than that caused by the 2016 event. The stress shadows mainly trend in the NNW-SSE and NEE-SWW direction, which released the stress on the western end of the HCSTF, the eastern end and western of the MYDMYF, the eastern end of the Sunan-Qilian fault, and the eastern Dabanshan fault. The stress loading zones show two directions, one of which forms two stress loading zones trending NNE-SSW, while the other of which is distributed along the TLSF and LLLF, with trends of NW and SE, strengthening the stress of the TLSE, the NLLLF, and the LLLF, implying a high possibility of strong earthquakes in the future (Figure 8c,d).

In the past few decades, moderate and strong earthquakes have rarely occurred along the Qilian-Haiyuan fault system. However, in recent years, moderate earthquakes with diverse focal mechanisms have frequently occurred on this strained fault system (Figure 2), such as the 2013 Mw5.1 Menyuan earthquake, the 2015 Mw5.2 Qilian earthquake, the 2016 Mw6.0 Menyuan earthquake, and the 2022 Mw6.6 Menyuan earthquake (Figures 1a and S6a). The enhanced earthquake clusters may indicate that the Qilian-Haiyuan fault system is more active than before. It is therefore imperative to strengthen the monitoring of crustal deformation in this region, which is helpful to quantify the strain accumulation prior to the earthquake.

4.3. The Slip Distribution Variations of the 2022 Menyuan Earthquake

After the occurrence of the 2022 Menyuan earthquake, seismogenic fault slip distributions have been studied by various researchers using InSAR observations and other data. Based on teleseismic waves and InSAR observations, He et al. [31] obtained a one-fault slip model of this event. Based on Sentinel-1 InSAR coseismic deformation, Luo et al. [34] sought a six-segment fault model and optimal dip angle of each segment using Bayesian method and SDM software, while Li et al. [32] built a double-segment fault model and obtained the best-fitting slip distribution by the particle swarm optimization method and Montecarlo analysis. The slip distribution given by them was much similar to our result. The fault coseismic slips are mostly confined above 12 km, with a maximum value of ~3.5 m at a depth of 2–5 km, and exist in shallow slip deficits. However, the coseismic slip of their results is shown as an asperity, while our slip model displays three asperities at depth, which may be related to the choice of sampling mode, inversion strategy, and fault parameters. Comparing the near-surface slip of slip models with the dislocation from the field survey [19], there are one and two large values on the west and east segment of our slip model, respectively, and the maximum displacement is located on the central segment, which is more consistent with the field survey than other research. Overall, we believe that our coseismic slip model may be more reasonable.

5. Conclusions

We investigated the pre-seismic deformation velocity field between 2014 and 2020 using Sentinel-1 data on the ascending track, and the coseismic deformation on both ascending and descending tracks associated with the Menyuan earthquakes in 2016 and 2022 by InSAR technique. Based on this, we inverted the fault geometric parameters and fine slip distribution of the two events and calculated the Δ CFS in the adjacent region caused by their coseismic deformation.

The InSAR observations and inversion results show that the seismogenic fault of the 2016 event is the NLLLF with a gentle dip, and its motion is thrust-dominated with a maximum slip of ~ 1 m; while the seismogenic fault of the 2022 event is the LLLF with a relatively steep dip, which is dominated by strike-slip components with a maximum slip of ~ 4 m and ruptured the surface. The coseismic Coulomb stress results suggest that the 2016 event had little influence on the occurrence of the 2022 event, and the LLLF and TLSF were in the stress-triggering zone of the 2022 event, indicating a high seismic risk on those faults, which need continuous attention.

Based on our slip model and other geophysical data, we infer that the NLLLF soles into the LLLF in the deep crust, forming a positive flower structure, which may have prevented the upwards propagation of the 2016 earthquake rupture, resulting in a shallow slip deficit, and the continuous accumulation of Coulomb stress may have increased the possibility of the occurrence of the 2022 earthquake.

Since the interseismic deformation field given in this paper includes the co- and post-seismic effects of the 2016 event, although they have little impact on the overall deformation analysis, a purer interseismic deformation field is needed in future. Moreover, the postseismic effects of the 1927 Ms8.0 Gulang and 1986 Mw6.0 Menyuan earthquakes, which occurred near there, have not been considered in this study, so further work should be carried out.

Supplementary Materials: The following supporting information can be downloaded at: <https://www.mdpi.com/article/10.3390/rs14246317/s1>. Figure S1: (a,b) observations, (e,f) predictions, and (i,j) residuals from the MYDMYF model of the 2016 event on the ascending and descending tracks, respectively. (c,d) Observations, (g,h) predictions, and (k,l) residuals from the one-fault model of the 2022 event. The solid red line marks the surface projections of the up-dip edge of the fault model. The black rectangle indicates the surface projection of the upper wall of the fault model. Figure S2: The relationship between coseismic Δ CFS and the aftershocks. (a,b) Δ CFS and aftershocks of the 2016 earthquake at depths 5 km and 10 km, (c,d) Δ CFS and aftershocks of the 2022 earthquake at depths 5 km and 10 km. The green circles are aftershocks that occurred near the corresponding depth (± 2.5 km), while the black dots represent aftershocks located at other depths. Figure S3: The magneto-telluric profiles along the Qilian-Haiyuan fault (modified from Zhao et al. [63]). Figure S4: The tectonic evolution and dynamic relationship between the NLLLF and LLLF (reprinted with permission from Guo et al., Science China Earth Sciences, published by Springer Nature, 2017 [36]). Figure S5: The topographic profiles near our study area. (a) The locations of the profile lines. The blue line indicates the profile line of Figure 10, while the magenta and orange lines indicate the profile line of Figure S5b, c. (b) The profile modified from Allen et al. [65]. (c) The profile modified from Gaudemer et al. [64]. HYF represents the Qilian-Haiyuan fault.

Author Contributions: All the authors participated in editing and reviewing the manuscript. methodology, D.W. and H.C.; validation, C.Q., D.Z. and X.S.; formal analysis, D.Z. and D.W.; investigation, D.Z.; data curation, D.W.; writing—original draft preparation, D.W.; writing—review and editing, D.Z. and C.Q.; visualization, D.W.; supervision, C.Q.; project administration, C.Q.; funding acquisition, C.Q. and X.S. All authors have read and agreed to the published version of the manuscript.

Funding: This research was funded by the National Key Laboratory of Earthquake Dynamics (LED2019A02), the National Natural Science Foundation of China (42174009), and the Basic Scientific Funding of Institute of Geology, China Earthquake Administration (IGCEA1809, IGCEA2104).

Acknowledgments: The Sentinel Synthetic Aperture Radar (SAR) data were downloaded from the ASF DAAC website (<https://search.asf.alaska.edu/#/home>, accessed on 18 January 2022). The

focal mechanisms were obtained from the Global Centroid Moment Tensor (GCMT; <https://www.globalcmt.org>, accessed on 16 June 2022), the U.S. Geological Survey (USGS; <https://earthquake.usgs.gov/earthquakes/>, accessed on 5 March 2022), and China Earthquake Networks Center (CENC; <https://news.ceic.ac.cn/index.html>, accessed on 5 March 2022). The seismic data were retrieved from China Earthquake Networks Center, National Earthquake Data Center (<http://data.earthquake.cn>, accessed on 30 December 2020). All figures were made using the Generic Mapping Tools software package v.5.4.3 [68].

Conflicts of Interest: The authors declare no conflict of interest.

References

1. Avouac, J.P.; Tapponnier, P. Kinematic Model of Active Deformation in Central-Asia. *Geophys. Res. Lett.* **1993**, *20*, 895–898. [[CrossRef](#)]
2. Zhang, P.Z.; Wang, Q.; Ma, Z.J. GPS velocity field and active crustal deformation in and around the Qinghai-Tibet Plateau. *Earth Sci. Front.* **2002**, *9*, 442–450. (In Chinese) [[CrossRef](#)]
3. Yuan, D.Y. Tectonic Deformation Features and Space-Time Evolution in Northeastern Margin of the Qinghai-Tibetan Plateau Since the Late Cenozoic Time. Ph.D. Thesis, Institute of Geology, CEA, Beijing, China, 2003. (In Chinese).
4. Li, Y.C.; Qu, C.Y.; Shan, X.J.; Song, X.G.; Zhang, G.H.; Gan, W.J.; Wen, S.Y.; Wang, Z.J. Deformation of the Haiyuan-Liupanshan fault zone inferred from the denser GPS observations. *Earthq. Sci.* **2015**, *28*, 319–331. [[CrossRef](#)]
5. Deng, Q.D.; Song, F.M.; Zhu, S.L.; Li, M.L.; Wang, T.L.; Zhang, W.Q.; Burchfiel, B.C.; Molnar, P.; Zhang, P.Z. Active faulting and Tectonics of the Ningxia-Hui Autonomous Region, China. *J. Geophys. Res.* **1984**, *89*, 4427–4445.
6. Zhang, P.Z.; Molnar, P.; Burchfiel, B.C.; Royden, L.; Wang, Y.P.; Deng, Q.D.; Song, F.M.; Zhang, W.Q.; Jiao, D.C. Bounds on the Holocene slip rate of the Haiyuan Fault, North-central China. *Quat. Res.* **1988**, *30*, 151–164. [[CrossRef](#)]
7. Burchfiel, B.C.; Zhang, P.Z.; Wang, Y.P.; Zhang, W.Q.; Song, F.M.; Deng, Q.D.; Molnar, P.; Royden, L. Geology of the Haiyuan Fault Zone, Ningxia-Hui Autonomous Region, China, and its relation to the evolution of the Northeastern Margin of the Tibetan Plateau. *Tectonics* **1991**, *10*, 1091–1110. [[CrossRef](#)]
8. Gan, W.J.; Zhang, P.Z.; Shen, Z.K.; Zheng, Z.J.; Wang, M.; Wan, Y.G.; Zhou, D.M.; Cheng, J. Present-day crustal motion within the Tibetan Plateau inferred from GPS measurements. *J. Geophys. Res.* **2007**, *112*. [[CrossRef](#)]
9. Thatcher, W. Microplate model for the present-day deformation of Tibet. *J. Geophys. Res.* **2007**, *112*. [[CrossRef](#)]
10. Wang, Y.Z.; Wang, M.; Shen, Z.K. Block-like versus distributed crustal deformation around the northeastern Tibetan Plateau. *J. Asian Earth Sci.* **2017**, *140*, 31–47. [[CrossRef](#)]
11. Jolivet, R.; Lasserre, C.; Doin, M.P.; Guillaso, S.; Peltzer, G.; Dailu, R.; Sun, J.; Shen, Z.K.; Xu, X. Shallow creep on the Haiyuan Fault (Gansu, China) revealed by SAR Interferometry. *J. Geophys. Res. Solid Earth* **2012**, *117*. [[CrossRef](#)]
12. Qu, C.Y.; Shan, X.J.; Xu, X.B.; Zhang, G.H.; Song, X.G.; Zhang, G.F. Near-field Motion of the Haiyuan Fault Zone in the Northeastern Margin of the Tibetan Plateau Derived from InSAR Permanent Scatterers Analysis. *J. Applied Remote Sens* **2013**, *7*, 073507. [[CrossRef](#)]
13. Daout, S.; Jolivet, R.; Lasserre, C.; Doin, M.P.; Barbot, S.; Tapponnier, P.; Peltzer, G.; Socquet, A.; Sun, J. Along-strike variations of the partitioning of convergence across the Haiyuan fault system detected by InSAR. *Geophys. J. Int.* **2016**, *205*, 536–547. [[CrossRef](#)]
14. Zhang, Y.F.; Shan, X.J.; Zhang, G.H.; Zhong, M.J.; Zhao, Y.J.; Wen, S.Y.; Qu, C.Y.; Zhao, D.Z. The 2016 Mw 5.9 Menyuan earthquake in the Qilian Orogen, China: A potentially delayed depth-segmented rupture following from the 1986 Mw 6.0 Menyuan earthquake. *Seismol. Res. Lett.* **2020**, *91*, 758–769. [[CrossRef](#)]
15. Li, Z.H.; Han, B.Q.; Liu, Z.J.; Zhang, M.M.; Yu, C.; Chen, B.; Liu, H.H.; Du, J.; Zhang, S.C.; Zhu, W.; et al. Source parameters and slip distributions of the 2016 and 2022 Menyuan, Qinghai earthquakes constrained by InSAR observations. *Geomat. Inf. Sci. Wuhan Univ.* **2022**, *47*, 887–897. (In Chinese) [[CrossRef](#)]
16. Hu, C.Z.; Yang, P.X.; Li, Z.M.; Huang, S.T.; Zhao, Y.; Chen, D.; Xiong, R.W.; Chen, Q.Y. Seismogenic mechanism of the 21 January 2016 Menyuan, Qinghai Ms6.4 earthquake. *Chin. J. Geophys.* **2016**, *59*, 1637–1646. (In Chinese) [[CrossRef](#)]
17. Wang, H.; Liu-Zeng, J.; Ng, A.H.M.; Ge, L.; Javed, F.; Long, F.; Aoudia, A.; Feng, J.; Shao, Z. Sentinel-1 observations of the 2016 Menyuan Earthquake: A buried reverse event linked to the left-lateral Haiyuan Fault. *Int. J. Appl. Earth Obs. Geoinf.* **2017**, *61*, 14–21. [[CrossRef](#)]
18. Liu, M.; Li, H.Y.; Peng, Z.G.; Ouyang, L.B.; Ma, Y.H.; Ma, J.X.; Liang, Z.J.; Huang, Y.F. Spatial-temporal distribution of early aftershocks following the 2016 Ms6.4 Menyuan, Qinghai, China earthquake. *Tectonophysics* **2019**, *766*, 469–479. [[CrossRef](#)]
19. Pan, J.W.; Li, H.B.; Chevalier, M.L.; Liu, D.L.; Li, C.; Liu, F.C.; Wu, Q.; Lu, H.J.; Jiao, L.Q. Coseismic surface rupture and seismogenic structure of the 2022 Ms6.9 Menyuan earthquake, Qinghai Province, China. *Acta Geol. Sin.* **2022**, *96*, 215–231. (In Chinese) [[CrossRef](#)]
20. Liu, J.H.; Hu, J.; Li, Z.W.; Ma, Z.F.; Shi, J.W.; Xu, W.B.; Sun, Q. Three-dimensional surface displacements of the 8 January 2022 Mw6.7 Menyuan earthquake, China from Sentinel-1 and ALOS-2 SAR observations. *Remote Sens.* **2022**, *14*, 1404. [[CrossRef](#)]
21. Chen, W.T.; Gan, W.J.; Xiao, G.R.; Wang, Y.B.; Lian, W.P.; Liang, S.M.; Zhang, K.L. Characteristics of regional crustal deformation before 2016 Menyuan Ms6.4 earthquake. *Geod. Geodyn.* **2016**, *7*, 275–283. [[CrossRef](#)]

22. Cui, D.X.; Qin, S.L.; Wang, W.P. Dynamics evolution of crustal deformation before the Ms6.4 Menyuan earthquake. *Geod. Geodyn.* **2016**, *7*, 253–260. [[CrossRef](#)]
23. Li, Y.S.; Jiang, W.L.; Zhang, J.F.; Luo, Y. Space geodetic observations and modeling of 2016 Mw 5.9 Menyuan earthquake: Implications on seismogenic tectonic motion. *Remote Sens.* **2016**, *8*, 519. [[CrossRef](#)]
24. Liu, Y.H.; Zhang, G.H.; Zhang, Y.F.; Shan, X.J. Source parameters of the 2016 Menyuan earthquake in the northeastern Tibetan Plateau determined from regional seismic waveforms and InSAR measurements. *J. Asian Earth Sci.* **2018**, *158*, 103–111. [[CrossRef](#)]
25. Zheng, B.W.; Gong, W.Y.; Wen, S.Y.; Zhang, Y.F.; Shan, X.J.; Song, X.G.; Liu, Y.H. Study on the seismogenic fault characteristics of 2016 Mw5.9 Menyuan earthquake based on Sentinel-1A data. *Seismol. Geol.* **2018**, *40*, 872–882. (In Chinese) [[CrossRef](#)]
26. Qu, W.; Liu, B.H.; Zhang, Q.; Gao, Y.; Chen, H.L.; Wang, Q.L.; Hao, M. Sentinel-1 InSAR observations of co- and post-seismic deformation mechanisms of the 2016 Mw 5.9 Menyuan earthquake, Northwestern China. *Adv. Space Res.* **2021**, *68*, 1301–1317. [[CrossRef](#)]
27. Han, S.; Wu, Z.H.; Gao, Y.; Lu, H.F. Surface rupture investigation of the 2022 Menyuan Ms 6.9 earthquake, Qinghai, China: Implications for the fault behavior of the Lenglongling Fault and regional intense earthquake risk. *J. Geomech.* **2022**, *28*, 155–168. (In Chinese) [[CrossRef](#)]
28. Fan, L.P.; Li, B.R.; Liao, S.R.; Jiang, C.; Fang, L.H. Precise relocation of the aftershock sequences of the 2022 M6.9 Menyuan earthquake. *Earthq. Sci.* **2022**, *35*, 138–145. [[CrossRef](#)]
29. Feng, W.P.; He, X.H.; Zhang, Y.P.; Fang, L.H.; Samsonov, S.; Zhang, P.Z. Seismic faults of the 2022 Mw6.6 Menyuan, Qinghai Earthquake and its implication for the regional seismogenic structures. *Sci. Bull.* **2022**, *617*, 1–17. (In Chinese) [[CrossRef](#)]
30. Yang, H.F.; Wang, D.; Guo, R.M.; Xie, M.Y.; Zang, Y.; Wang, Y.; Yao, Q.; Cheng, C.; An, Y.R.; Zhang, Y.Y. Rapid report of the 8 January 2022 Ms 6.9 Menyuan earthquake, Qinghai, China. *Earthq. Res. Adv.* **2022**, *2*, 100113. [[CrossRef](#)]
31. He, P.; Liu, C.L.; Wen, Y.M.; He, X.P.; Ding, K.H.; Xu, C.J. The 2022 Mw6.6 Menyuan Earthquake in the Northwest Margin of Tibet: Geodetic and Seismic Evidence of the Fault Structure and Slip Behavior of the Qilian–Haiyuan Strike-Slip Fault. *Seismol. Res. Lett.* **2022**. [[CrossRef](#)]
32. Li, Y.S.; Jiang, W.L.; Li, Y.J.; Shen, W.H.; He, Z.T.; Li, B.Q.; Li, Q.; Jiao, Q.S.; Tian, Y.F. Coseismic Rupture Model and Tectonic Implications of the January 7 2022, Menyuan Mw 6.6 Earthquake Constraints from InSAR Observations and Field Investigation. *Remote Sens.* **2022**, *14*, 2111. [[CrossRef](#)]
33. Liu, L.; Liu, X.W.; Zhang, B.; He, W.G.; Zhu, J.W.; Cai, Y.M. Recognition of surface ruptures of Menyuan Ms6.9 earthquake using GF images. *China Earthq. Eng. J.* **2022**, *44*, 440–449. (In Chinese) [[CrossRef](#)]
34. Luo, H.; Wang, T. Strain Partitioning on the Western Haiyuan Fault System Revealed by the Adjacent 2016 Mw5.9 and 2022 Mw6.7 Menyuan Earthquakes. *Geophys. Res. Lett.* **2022**, *49*, e2022GL099348. [[CrossRef](#)]
35. Xu, X.W.; Han, Z.J.; Yang, X.P.; Zhang, S.M.; Yu, G.H.; Zhou, B.G.; Li, F.; Ma, B.Q.; Chen, G.H.; Ran, Y.K. *Seismotectonic Map in China and Its Adjacent Regions*; Seismological Press: Beijing, China, 2016. (In Chinese) [[CrossRef](#)]
36. Guo, P.; Han, Z.J.; An, Y.F.; Jiang, W.L.; Mao, Z.B.; Feng, W. Activity of the Lenglongling Fault System and seismotectonics of the 2016 Ms6.4 Menyuan earthquake. *Sci. China Earth Sci.* **2017**, *47*, 617–630. [[CrossRef](#)]
37. Wang, M.; Shen, Z.K. Present-day crustal deformation of continental China derived from GPS and its tectonic implications. *J. Geophys. Res. Solid Earth* **2020**, *125*, e2019JB018774. [[CrossRef](#)]
38. Wei, C.M. Study of the Present Crustal Deformation Characteristics of the Southwest Margin of Ordos Block Were Using GPS. Ph.D. Thesis, Lanzhou Institute of Seismology, CEA, Lanzhou, China, 2020. (In Chinese).
39. Rosen, P.A.; Gurrola, E.; Sacco, G.F.; Zebker, H. The InSAR Scientific Computing Environment. In Proceedings of the EUSAR 2012 9th European Conference on Synthetic Aperture Radar, Nuremberg, Germany, 23–26 April 2012.
40. Hooper, A.; Bekaert, D.; Spaans, K.; Arikani, M. Recent advances in SAR Interferometry time series analysis for measuring crustal deformation. *Tectonophysics* **2012**, *514–517*, 1–13. [[CrossRef](#)]
41. Catalão, J.; Nico, G.; Hanssen, R.; Catita, C. Merging GPS and atmospherically corrected InSAR data to map 3-D terrain displacement velocity. *IEEE Trans. Geosci. Remote Sens.* **2011**, *49*, 2354–2360. [[CrossRef](#)]
42. Hu, J.; Li, Z.W.; Ding, X.L.; Zhu, J.J.; Sun, Q. Derivation of 3-D coseismic surface displacement fields for the 2011 Mw 9.0 Tohoku-Oki earthquake from InSAR and GPS measurements. *Geophys. J. Int.* **2013**, *192*, 573–585. [[CrossRef](#)]
43. Wegmüller, U.; Werner, C.; Strozzi, T.; Wiesmann, A.; Frey, O.; Santoro, M. Sentinel-1 support in the GAMMA Software. *Procedia Comput. Sci.* **2016**, *100*, 1305–1312. [[CrossRef](#)]
44. Michel, R.; Avouac, J.P.; Taboury, J. Measuring ground displacements from SAR amplitude images: Application to the Landers earthquake. *Geophys. Res. Lett.* **1999**, *26*, 875–878. [[CrossRef](#)]
45. Strozzi, T.; Luckman, A.; Murray, T.; Wegmüller, U.; Werner, C. Glacier motion estimation using SAR offset-tracking procedures. *IEEE Trans. Geosci. Remote Sens.* **2002**, *40*, 2384–2391. [[CrossRef](#)]
46. Li, Y.B.; Gan, W.J.; Wang, Y.B.; Chen, W.T.; Liang, S.M.; Zhang, K.L.; Zhang, Y.Q. Seismogenic structure of the 2016 Ms6.4 Menyuan earthquake and its effect on the Tianzhu seismic gap. *Geod. Geodyn.* **2016**, *7*, 230–236. [[CrossRef](#)]
47. Wang, R.J.; Diao, F.Q.; Hoehner, A. SDM-A geodetic inversion code incorporating with layered crust structure and curved fault geometry. In Proceedings of the European Geosciences Union Conference, Vienna, Austria, 7–12 April 2013. Vienna: EGU General Assembly 2013: Number EGU2013-2411-1.
48. Persson, P.O.; Strang, G. A simple Mesh Generator in MATLAB. *Siam Rev.* **2004**, *46*, 329–345. [[CrossRef](#)]

49. Xu, J.; Shao, Z.G.; Zhang, L.P.; Ma, H.S. Progress and review of Coulomb failure stress changes on fault plane. *Prog. Geophys.* **2013**, *28*, 132–145. (In Chinese) [[CrossRef](#)]
50. Stein, R.S.; King, G.C.P.; Lin, J. Change in failure stress on the southern San Andreas fault system caused by the 1992 Magnitude=7.4 Landers earthquake. *Science* **1992**, *258*, 1328–1332. [[CrossRef](#)] [[PubMed](#)]
51. Toda, S.; Lin, J.; Meghraoui, M.; Stein, R.S. 12 May 2008 M=7.9 Wenchuan, China, earthquake calculated to increase failure stress and seismicity rate on three major fault systems. *Geophys. Res. Lett.* **2008**, *35*. [[CrossRef](#)]
52. Chen, W.; Qiao, X.J.; Liu, G.; Xiong, W.; Jia, Z.G.; Li, Y.; Wang, Y.B.; You, X.Z.; Long, F. Study on the coseismic slip model and Coulomb stress of the 2017 Jiuzhaigou Ms7.0 earthquake constrained by GNSS and InSAR measurements. *Chin. J. Geophys.* **2018**, *61*, 2122–2132. (In Chinese) [[CrossRef](#)]
53. Zhu, A.Y.; Wang, Y.Z.; Li, Y.H.; Zhang, D.N. Numerical simulation on the mechanism of the Madoi, Qinghai Ms7.4 earthquake constrained by InSAR deformation. *Chin. J. Geophys.* **2021**, *64*, 4548–4561. (In Chinese) [[CrossRef](#)]
54. Harris, R.A. Introduction to special section: Stress triggers, stress shadows, and implications for seismic hazard. *J. Geophys. Res.* **1998**, *103*, 24347–24358. [[CrossRef](#)]
55. Stein, R.S. The role of stress transfer in earthquake occurrence. *Nature* **1999**, *402*, 605–609. [[CrossRef](#)]
56. Wang, R.J.; Lorenzo-Martin, F.L.; Roth, F. PSGRN/PSCMP—A new code for calculating co- and post-seismic deformation, geoid and gravity changes based on the viscoelastic-gravitational dislocation theory. *Comput. Geosci.* **2006**, *32*, 527–541. [[CrossRef](#)]
57. King, G.C.P.; Stein, R.S.; Lin, J. Static stress changes and the triggering of earthquakes. *Bull. Seismol. Soc. Am.* **1994**, *84*, 935–953. [[CrossRef](#)]
58. Zhang, R.; Zhang, Z.Q.; Zheng, D.W.; Liu, X.W.; Lei, Q.Y.; Shao, Y.X. Coulomb stress transfer of strong earthquakes within tectonic belts near western Ordos blocks. *Chin. J. Geophys.* **2021**, *64*, 3576–3599. (In Chinese) [[CrossRef](#)]
59. Shi, F.Q.; Shao, Z.G.; Zhan, W.; Ding, X.G.; Zhu, L.; Li, Y.J. Numerical modeling of the shear modulus and stress state of active faults in the northeastern margins of the Tibetan Plateau. *Chin. J. Geophys.* **2018**, *61*, 3651–3663. (In Chinese) [[CrossRef](#)]
60. Gao, R.; Wang, H.Y.; Yin, A.; Dong, S.W.; Kuang, Z.Y.; Zuza, A.V.; Li, W.H.; Xiong, X.S. Tectonic development of the Northeastern Tibetan Plateau as constrained by high-resolution deep seismic-reflection data. *Lithosphere* **2013**, *5*, 555–574. [[CrossRef](#)]
61. Zhao, L.Q.; Zhan, Y.; Sun, X.Y.; Hao, M.; Zhu, Y.Q.; Chen, X.B.; Yang, H. The hidden seismogenic structure and dynamic environment of the 21 January Menyuan Qinghai, Ms6.4 earthquake derived from magnetotelluric imaging. *Chin. J. Geophys.* **2019**, *62*, 2088–2100. (In Chinese) [[CrossRef](#)]
62. Zhao, L.Q.; Zhan, Y.; Wang, Q.L.; Sun, X.Y.; Hao, M.; Zhu, Y.Q.; Han, J. The deep electrical structure and seismogenic background of Lenglongling uplift and its adjacent areas in the eastern end of Qilian Mountains. *Chin. J. Geophys.* **2020**, *63*, 1014–1025. (In Chinese) [[CrossRef](#)]
63. Zhao, L.Q.; Sun, X.Y.; Zhan, Y.; Yang, H.B.; Wang, Q.L.; Hao, M.; Liu, X.H. The seismogenic model of the Menyuan Ms6.9 earthquake on January 8, 2022, Qinghai Province and segmented extensional characteristics of the Lenglongling fault. *Chin. J. Geophys.* **2022**, *65*, 1536–1546. (In Chinese) [[CrossRef](#)]
64. Gaudemer, Y.; Tapponnier, P.; Meyer, B.; Peltzer, G.; Guo, S.M.; Chen, Z.T.; Dai, H.G.; Cifuentes, I. Partitioning of crustal slip between linked, active faults in the eastern Qilian Shan, and evidence for a major seismic gap, the ‘Tianzhu gap’, on the western Haiyuan Fault, Gansu (China). *Geophys. J. Int.* **1995**, *120*, 599–645. [[CrossRef](#)]
65. Allen, M.B.; Walters, R.J.; Song, S.G.; Saville, C.; Paola, N.D.; Ford, J.; Hu, Z.X.; Sun, W.L. Partitioning of oblique convergence coupled to the fault locking behavior of fold-and-thrust belts: Evidence from the Qilian Shan, northeastern Tibetan Plateau. *Tectonics* **2017**, *36*, 1679–1698. [[CrossRef](#)]
66. Elliott, J.R.; Parsons, B.; Jackson, J.A.; Shan, X.; Sloan, R.A.; Walker, R.T. Depth segmentation of the seismogenic continental crust: The 2008 and 2009 Qaidam earthquakes. *Geophys. Res. Lett.* **2011**, *38*. [[CrossRef](#)]
67. Wen, S.Y.; Shan, X.J.; Zhang, Y.F.; Wang, J.Q.; Zhang, G.H.; Qu, C.Y.; Xu, X.B. Three-dimensional co-seismic deformation of the Da Qaidam, Qinghai earthquakes derived from D-InSAR data and their source features. *Chin. J. Geophys.* **2016**, *59*, 912–921. (In Chinese) [[CrossRef](#)]
68. Wessel, P.; Smith, W.H. New, improved version of Generic Mapping Tools released. *Eos Trans. AGU* **1998**, *79*, 579. [[CrossRef](#)]